Journal of Oncology Research and Therapy
Angel I, et al. Oncol Res Ther 11: 10350.
www.doi.org/10.29011/2574-710X.10350
www.gavinpublishers.com

OPEN ACCESS

GAVIN PUBLISHERS

Research Article

Telomir-Zn Modulates Intracellular Iron and Copper to Inhibit JmjC Histone Demethylases and Suppress Tumor Growth in Prostate and Triple-Negative Breast Cancer

Itzchak Angel[1]*, Micha Gladnikoff[2], Perri Rozenberg Hasson[3], Gabriela Vazquez Rodriguez[4], Raphael Mayer[2], Anna Erkstam[4], Erez Aminov[1]

[1]Telomir Pharmaceuticals, Inc., Miami, FL, United States.

[2]Smart Assays Biotechnologies, Nes-Ziona, Israel.

[3]Pharmaseed Ltd., Nes-Ziona, Israel.

[4]BioReperia AB, Linköping, Sweden.

***Corresponding author:** Angel I, Telomir Pharmaceuticals, Inc., Miami, FL, United States.

Citation: Angel I, Gladnikoff M, Hasson PR, Rodriguez GV, Mayer R, et al. (2026) Telomir-Zn Modulates Intracellular Iron and Copper to Inhibit JmjC Histone Demethylases and Suppress Tumor Growth in Prostate and Triple-Negative Breast Cancer. J Oncol Res Ther 11: 10350. DOI: 10.29011/2574-710X.10350.

Received Date: 27 July, 2026; **Accepted:** 03 August, 2026; **Published Date:** 06 August, 2026.

Abstract

Dysregulated labile intracellular Fe^{2+} and Cu^{2+} pools fuel oxidative stress and sustain the activity of Fe^{2+}-dependent Jumonji C (JmjC) histone demethylases (KDM2, KDM5, and KDM6 families), promoting oncogenic epigenetic states and silencing of tumor-suppressor genes in multiple cancers. Telomir-Zn (2,4,6-tris(3,4-dihydro-2H-pyrrol-2-yl)pyridine, ZnCl2) is a first-in-class small-molecule modulator with preferential affinity for labile Cu^{2+} > Fe^{2+} >> Zn^{2+}. It rapidly depletes intracellular labile Fe^{2+}, inhibits multiple JmjC-domain histone demethylases, and induces epigenetic reprogramming.

In biochemical and cellular studies, Telomir-Zn exhibited faster and more potent intracellular Fe^{2+} depletion than deferoxamine, with selective cytotoxicity in iron-dependent cancer models. Iron supplementation significantly rescued viability, confirming on-target activity. In an aggressive PC-3 prostate cancer xenograft model, oral Telomir-Zn produced tumor growth suppression and significantly reduced DNA hypermethylation of key tumor-suppressor genes (STAT1, GSTP1, RASSF1A, CDKN2A, MASPIN, CASP8) without affecting telomere length. In triple-negative breast cancer (TNBC) models, Telomir-Zn suppressed proliferation across multiple cell lines in an iron-dependent manner and reduced primary tumor growth in BT-549 and HCC1806 zebrafish xenografts, with additional anti-metastatic effects in HCC1806. Combination with paclitaxel enhanced efficacy in both models.

These results establish selective intracellular metal modulation as a novel therapeutic strategy that links redox-metal homeostasis to epigenetic reprogramming and tumor suppression in iron-addicted malignancies. Telomir-Zn represents a promising orally bioavailable candidate for the treatment of prostate cancer and TNBC, supporting further clinical development.

Citation: Angel I, Gladnikoff M, Hasson PR, Rodriguez GV, Mayer R, et al. (2026) Telomir-Zn Modulates Intracellular Iron and Copper to Inhibit JmjC Histone Demethylases and Suppress Tumor Growth in Prostate and Triple-Negative Breast Cancer. J Oncol Res Ther 11: 10350. DOI: 10.29011/2574-710X.10350.

Keywords: Intracellular Iron/Copper Modulation; Jmjc Histone Demethylases; Epigenetic Reprogramming; Iron Addiction; DNA Methylation; Prostate Cancer; Triple-Negative Breast Cancer; Zebrafish Xenograft.

Graphical Abstract

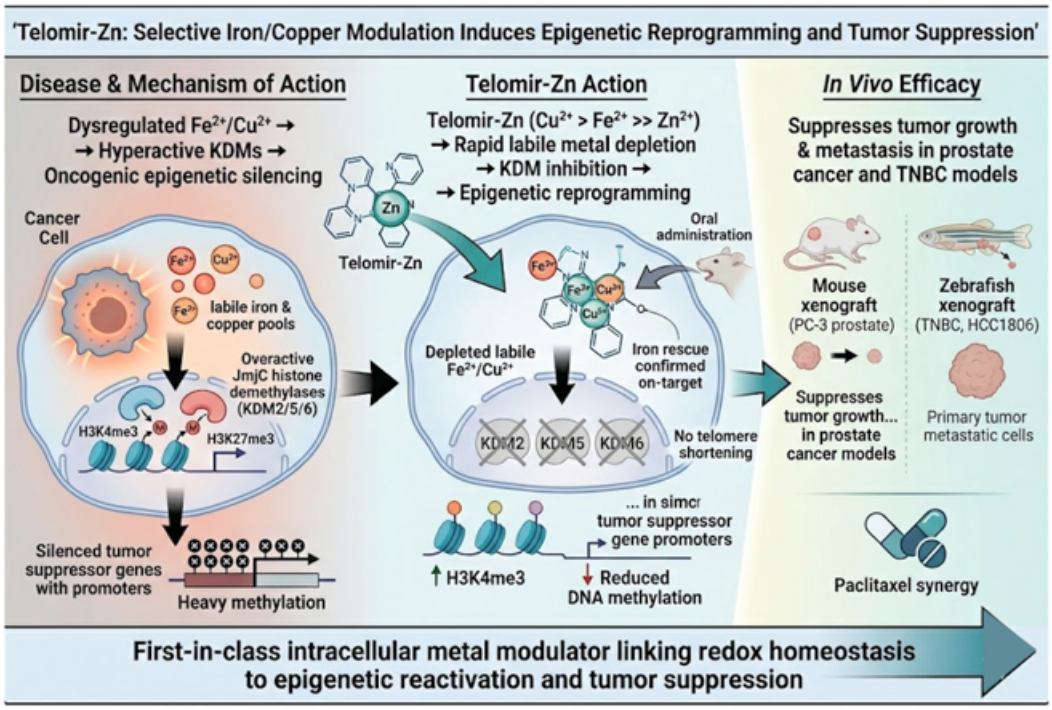

Introduction

Epigenetic dysregulation is a central driver of cancer initiation and progression, enabling tumor cells to silence tumor-suppressor genes, evade immune surveillance, and acquire phenotypes associated with genomic instability and therapeutic resistance [1-3].

Aberrant promoter hypermethylation of genes such as STAT1, GSTP1, RASSF1A, CDKN2A, and MASPIN is well-documented across multiple malignancies and contributes to unchecked proliferation, loss of apoptosis, impaired detoxification, altered immune signaling, and enhanced metastatic potential [2-6]. These epigenetic abnormalities frequently coexist with dysregulated metal ion homeostasis, particularly elevated intracellular iron and copper, which further promotes tumor progression through increased reactive oxygen species (ROS), DNA damage, and metabolic reprogramming [7-9]. Emerging evidence indicates that these epigenetic abnormalities frequently coexist with dysregulated intracellular metal homeostasis, suggesting a functional link between metal availability and chromatin regulation in cancer.

Iron and copper are essential transition metals that play fundamental roles in cellular metabolism, redox balance, and signaling. Beyond these canonical functions, iron and copper serve as critical cofactors for multiple chromatin-modifying enzymes that directly regulate epigenetic state and transcriptional programs. In particular, Fe^{2+}-dependent Jumonji C (JmjC) histone demethylases—including members of the KDM2, KDM5, and KDM6 families—require intracellular ferrous iron for catalytic activity and are frequently overexpressed or hyperactive in aggressive malignancies [10-14]. Dysregulation of these enzymes supports oncogenic transcriptional programs, stem-like states, immune evasion, and resistance to therapy.

Unlike direct epigenetic inhibitors such as DNA methyltransferase (DNMT) or histone deacetylase (HDAC) inhibitors, modulation of intracellular metal availability represents an indirect yet coordinated strategy to regulate multiple epigenetic enzymes simultaneously. Tumors characterized by elevated labile iron pools and heightened reliance on Fe^{2+}-dependent epigenetic enzymes therefore represent a biologically defined, iron-dependent phenotype that may be particularly vulnerable to intracellular metal modulation [7, 15-17].

Telomir-Zn (2,4,6-tris (3,4-dihydro-2H-pyrrol-2-yl) pyridine, ZnCl2) is a newly developed small-molecule modulator of in-

tracellular iron and copper designed to selectively regulate labile metal pools while largely sparing zinc, a critical structural cofactor for numerous tumor-suppressor proteins and transcription factors. Unlike classical high-affinity chelators, Telomir-Zn exhibits low-molar chelation efficiency, enabling limited compound exposure to modulate disproportionately larger intracellular metal pools. Given the convergence of metal dysregulation, epigenetic silencing, and cancer progression, we investigated the mechanism of action of Telomir-Zn using biochemical assays, cancer cell models, and an aggressive PC-3 prostate cancer xenograft model.

Triple-negative breast cancer (TNBC) is a clinically aggressive subtype of breast cancer defined by the absence of estrogen receptor (ER), progesterone receptor (PR), and HER2 expression. TNBC accounts for approximately 15–20% of breast cancer diagnoses and is characterized by high histological grade, an increased risk of early recurrence, and poorer clinical prognosis compared with other breast cancer subtypes [18, 19]. Although TNBC lacks the hormone-receptor– and HER2-directed therapies available in other breast cancer subtypes, recent approvals—including PD-1/PD-L1 immune checkpoint inhibitors in biomarker-selected disease, the Trop-2 antibody–drug conjugate sacituzumab govitecan and PARP inhibitors for BRCA-mutated tumors have expanded the landscape. Nonetheless, systemic chemotherapy remains a backbone of treatment for many patients, and durable responses are limited, highlighting the continued need for new therapeutic strategies. Although initial responses are often observed, therapeutic resistance and metastatic progression frequently occur, highlighting the need for new therapeutic strategies. Recent studies suggest that metabolic dependencies represent promising therapeutic targets in TNBC. Among these, dysregulated iron metabolism has emerged as a hallmark of many aggressive cancers. Tumor cells frequently expand their intracellular labile iron pool to sustain mitochondrial respiration, DNA synthesis, and metabolic activity required for rapid proliferation [20, 21].

TNBC cells, particularly those with metastatic potential, exhibit increased copper uptake and retention compared to non-metastatic or less aggressive breast cancer subtypes. This “copper addiction” phenotype renders TNBC particularly vulnerable to copper depletion strategies. Clinical and preclinical studies have shown that pharmacological copper chelation (e.g., with tetrathiomolybdate) reduces mitochondrial OXPHOS, impairs metastatic colonization, and prolongs metastasis-free survival in high-risk TNBC patients without significantly affecting primary tumor growth [22, 23].

TNBC and castration-resistant prostate cancer represent particularly aggressive subtypes with limited targeted options and high rates of metastasis and chemoresistance. Both malignancies frequently exhibit ‘iron addiction’ characterized by expanded labile iron pools that support rapid proliferation, metabolic reprogramming, and epigenetic plasticity. We hypothesized that selective modulation of intracellular labile Fe^{2+} and Cu^{2+} by Telomir-Zn would simultaneously disrupt JmjC KDM activity, reverse tumor-suppressor gene silencing, and suppress tumor progression in these iron-dependent cancers. To test this, we integrated comprehensive biochemical and mechanistic studies with efficacy evaluation in a PC-3 prostate cancer mouse xenograft model and multiple TNBC cell lines plus zebrafish xenografts, including iron-rescue experiments and combination with paclitaxel. This dual-model approach addresses both mechanistic depth and translational relevance across iron-dependent solid tumors.

Results

Telomir-Zn possesses a novel tri-pyrrole–pyridine structure that enables metal-ion chelation (Fig 1). The compound has been developed as the $ZnCl_2$ salt conjugate (Telomir-Zn or Zn-Telomir).

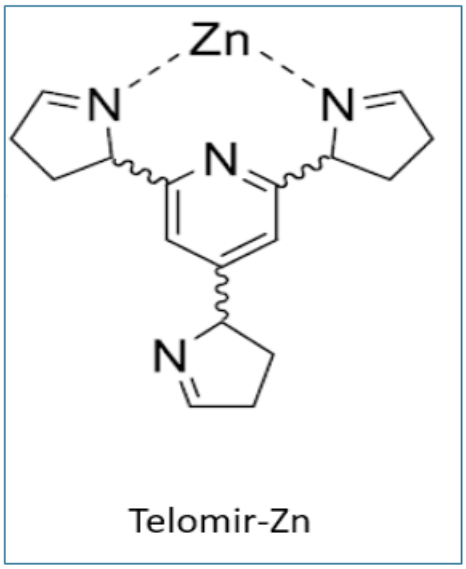

Figure 1: Structure of Telomir-Zn.

Biochemical Characterization of Metal-Binding Properties

Telomir-Zn chelation of Fe^{2+} was characterized using a Ferene-based colorimetric assay, as adapted from Abbasi et al. 2021 [24]. The method enables measurement of the labile/free iron pool. Ferene specifically chelates ferrous iron (Fe^{2+}) to form a stable complex that is detected spectrophotometrically. Chelation of Fe^{2+} by the test compounds was measured by the reduction in concentration of free Fe^{2+} available to be detected with Ferene. The relative Fe^{2+}-binding affinities of Telomir-Zn was compared with the established iron chelator deferoxamine (DFO).

Results in Figure 2 present a representative outcome of the Fe^{2+} chelation assay. Fe^{2+} was maintained at 20 μM, and Telomir-Zn

and DFO chelators were titrated over a concentration range of 3–50 µM. Both compounds tested reduced the concentration of free Fe^{2+} in a dose-dependent manner, with distinct efficiencies as reflected by the differing slopes of the fitted responses. These data demonstrate that Telomir compounds chelate Fe^{2+} effectively, although with lower apparent affinity than DFO under the assay conditions. Under these experimental conditions Telomir-Zn binds Fe^{2+} at a ratio of approximately 2:1 (Tel-Zn: Fe^{2+}), whereas DFO binds Fe^{2+} in an approximate equimolar ratio. This is in accordance with scientific literature [25].

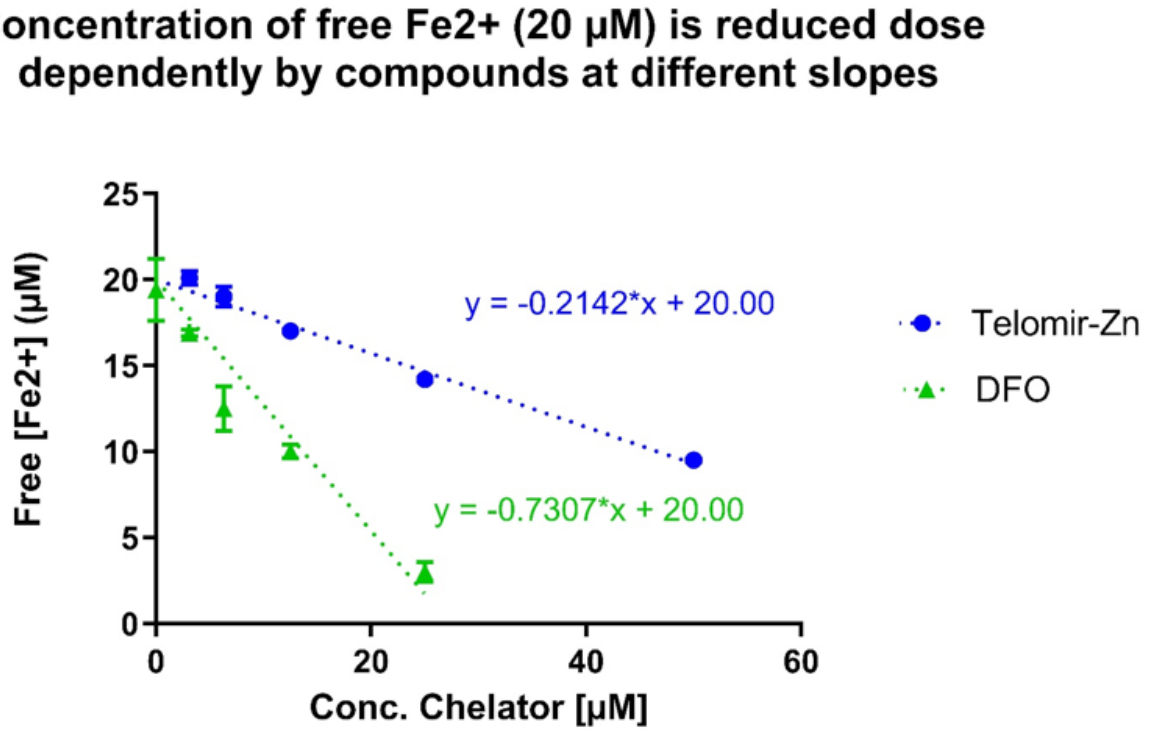

Figure 2. Comparative Effects of Telomir-Zn and DFO on Free Fe^{2+} Concentration. Data represents the mean of three replicate measures.

A competitive binding assay was employed to determine the relative affinities of Telomir-Zn or DFO for Fe^{2+}, Cu^{2+}, and Zn^{2+} ions. Telomir or DFO (100 µM) were incubated with Fe^{2+} (100 µM) in the presence of varying concentrations of a competing ion (3–200 µM). Samples without chelator were included as controls to confirm that Cu^{2+} and Zn^{2+} do not interfere with Fe^{2+} detection by Ferene.

Results in Figure 3A show that Telomir-Zn (100 µM) chelated a fraction of Fe^{2+}, decreasing the Ferene-detectable free Fe^{2+} by ~25% relative to the Fe^{2+}-only control. Upon titration with Cu^{2+}, free Fe^{2+} increases in a concentration-dependent manner, and at 100 µM Cu^{2+} the free Fe^{2+} level approaches control values. Cu^{2+} alone did not affect Ferene-based Fe^{2+} quantification, indicating that the observed recovery reflects metal competition rather than assay interference. These data imply a higher apparent affinity of Telomir-Zn for Cu^{2+} than for Fe^{2+}.

In contrast, Figure 3B shows that Zn^{2+} did not measurably alter free Fe^{2+} in the presence of Telomir-Zn over the tested concentration range. The control, Zn^{2+}-only, similarly shows no interference with Ferene detection. Thus, the Fe^{2+}–Telomir-Zn interaction is selectively perturbed by Cu^{2+} but not by Zn^{2+}.

In comparison, Figures 3A–3B show that DFO (100 µM) strongly chelated Fe^{2+}, lowering free Fe^{2+} by ~60%. Neither Cu^{2+} nor Zn^{2+} reversed this effect, indicating negligible competition with Fe^{2+} for DFO under these conditions and supporting a substantially higher affinity of DFO for Fe^{2+} than for Cu^{2+} or Zn^{2+} [22, 23].

Taken together, the results suggest that Telomir-Zn displays selective metal ion binding with the apparent affinity order Cu^{2+} > Fe^{2+} > Zn^{2+}, whereas DFO exhibits strong selectivity for Fe^{2+} in this assay.

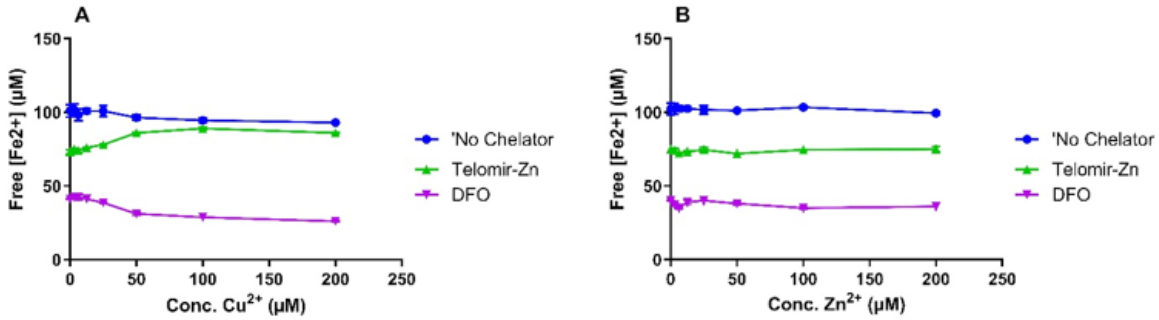

Figure 3: Competition Analysis Between Cu^{2+} and Zn^{2+} on Free Fe^{2+}. A. Competition with Copper. B. Competition with Zinc. Data represents mean of three replicate measures.

Intracellular Fe^{2+} Quantification by FerroOrange Staining

The effect of Telomir-Zn on intracellular labile Fe^{2+} levels was characterized using the stain FerroOrange [26]. HaCaT cells were treated with Telomir-Zn and DFO at a range of concentrations (0.25 μM -5 μM) and intracellular Fe^{2+} levels were assessed at different time-points (3–24 hours).

Untreated cells exhibited intense and stable intracellular Fe^{2+} staining (Figure 4). At lower magnification (4x) samples displayed dense, heterogeneous iron-associated fluorescence across the entire field. Using higher magnification (10x), the untreated cells showed pronounced intracellular iron-rich structures. In contrast, cells treated with Telomir-Zn (1 μM, 24 h) had low fluorescence indicating minimal intracellular free Fe^{2+} levels.

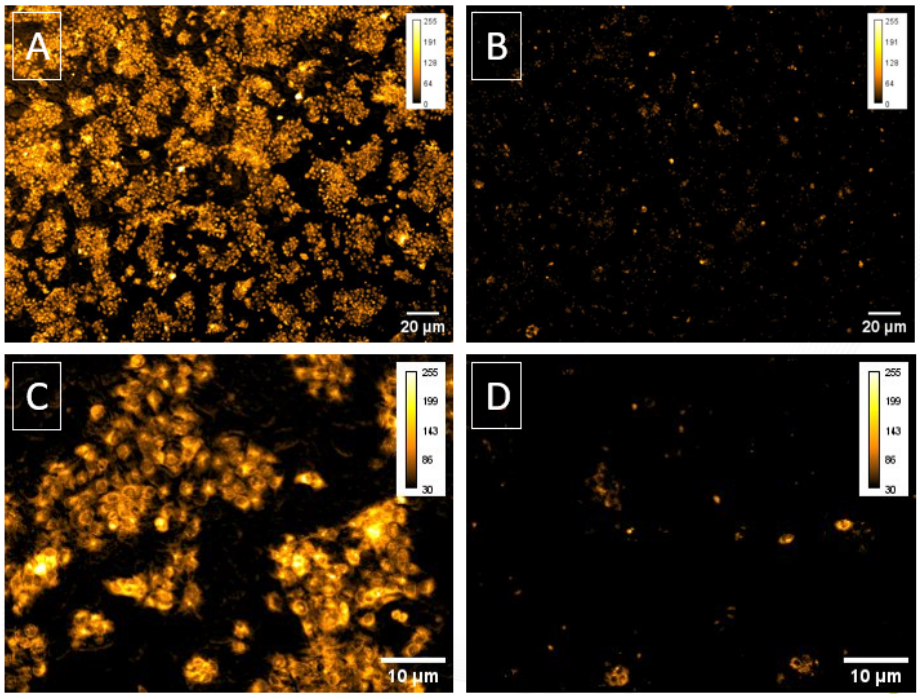

Figure 4: Fluorescent Microscopy Showing Effect of Telomir-Zn (at 1μM) on Intracellular Fe^{2+} Concentration in HaCaT Cells at Two Magnifications: A (5x) and C (10x) untreated cells; Cells treated with Telomir-Zn. B (5x) and D (10x).

5x Exposure 270 ms, Scalebar 20 μm; 10x Exp. 240 ms, Scalebar 10 μm.

Fluorescence microscopy and measurement by plate reader of stained HaCaT cells showed that Telomir-Zn and DFO each reduced the intracellular labile Fe^{2+} pool in a time- and dose-dependent manner, with distinct efficiencies and temporal profiles. Qualitatively, both Telomir compounds reduced intracellular Fe^{2+} more rapidly than DFO, most notably at the early 3 h and 6 h time points. A time and concentration–response analysis further confirmed dose-dependent Fe^{2+} depletion, with Telomir compounds exhibiting a greater effect than DFO over the tested range. Across assays, compound efficacy followed the order Telomir-Zn > DFO, most evident at 1–2 µM.

Kinetic analysis revealed that the majority of Fe^{2+} reduction induced by Telomir-Zn occurred within the initial hours of treatment, whereas DFO produced a slower, near-linear decrease over the same interval. At later time points, the rate of Fe^{2+} reduction by the Telomir compounds converged toward that of DFO (Figure 5). For this analysis intensity was normalized to untreated samples at each timepoint.

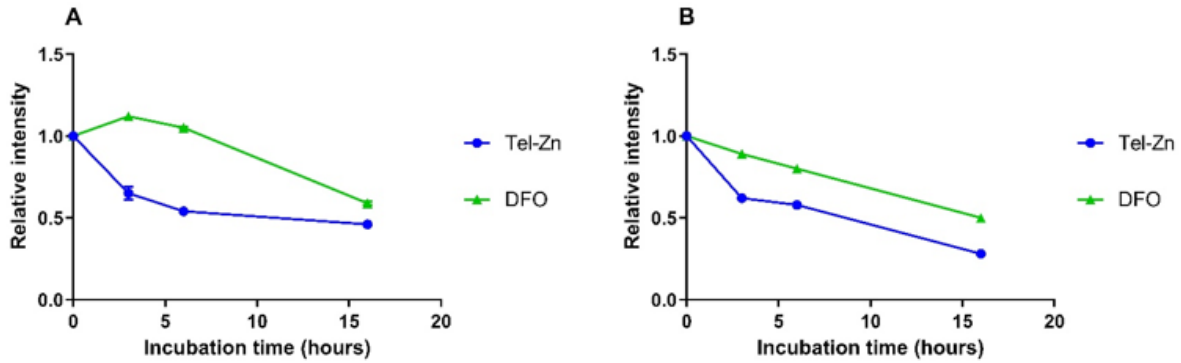

Figure 5: Relative Fluorescence Intensity of Intracellular Fe2+ at Different Time Points, as a Function of the Chelator Used.

Intensity was normalized to untreated samples at each timepoint. A. All chelators at 1 µM. B. All chelators at 2 µM. Data represents the mean of three replicate measures.

Quantification of FerroOrange fluorescence by plate reader enabled calculation of IC_{50} values as function of incubation time (see table 1). Across incubation periods, potency followed the order Telomir-Zn > DFO, indicating higher apparent cellular efficacy of Telomir-Zn compared with DFO.

	IC_{50} values (µM)		
Incubation Time (h)	**3**	**6**	**16**
Telomir-Zn	1.5	1.05	0.83
DFO	23.4	24.6	1.52

Table 1: Comparative IC_{50} Values (µM) for Reduction of Intracellular Fe^{2+} Fluorescence.

Representative microscopy images illustrate dose-dependent (0.5–2 µM) reduction in FerroOrange fluorescence as a function of treatment with Telomir-Zn and DFO for 16 hours (Figure 6). Cells treated with DFO showed a strong intensity at 0.5 µM which was gradually reduced at the higher concentrations. Treatment with 0.5 µM Telomir-Zn reduced intensity efficiently indicating significant reduction of intracellular iron. Increase of the Telomir-Zn concentration further reduces the fluorescent intensity. At all tested concentrations, Telomir-Zn reduced FerroOrange fluorescence more efficiently than deferoxamine.

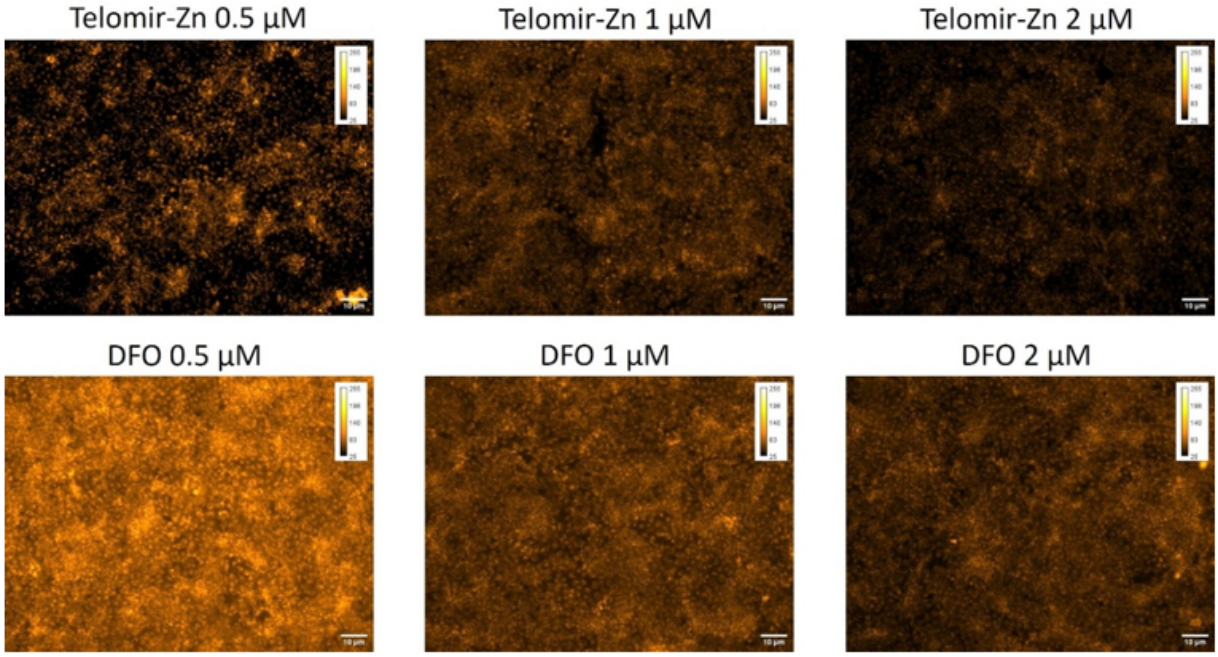

Figure 6: Comparative Effects of Telomir-Zn to DFO at 16 hours. Imaged at 10x magnification and exposure 150 ms exposure.

Telomir-Zn Selectively Reduces Cancer Cell Viability in Iron-Dependent Models

Cytotoxicity was assessed at 24–72 h after Telomir-Zn exposure in different cell lines, and the IC_{50} values of viability, were determined using modified methods. Microscopic inspection and functional tests at 24 h revealed only minor viability changes, limited to concentrations above 10µM. For selected cell lines, extended incubations (96 h) produced a more pronounced loss of viability at toxic doses, resulting in modestly lower IC_{50} estimates, while the highest non-toxic concentration remained unchanged.

Across the tested cell lines, Telomir-Zn showed cell type–dependent cytotoxicity at 48- and 72-hours, with clear differences in apparent potency (IC_{50}) and tolerated dose ranges. HCC1806, MDA-MB-468 (TNBC) and HL-60 (leukemia) cells were the most sensitive (Table 2).

Cell line used	**Cancer Type**	**Telomir-Zn**
		IC_{50} (µM)
HCC 1806	TNBC	0.87
MDA-MB-468		1.5
HCC 70		3.6
HL-60	Leukemia	1.6
PC-3	Prostate (Androgen-independent)	14.3
LNCap	Prostate (Androgen-dependent)	21.3
PANC-1	Pancreatic	38.6
HaCaT	Normal keratinocytes	>50

Table 2. Anti-Cancer Activities of Telomir-Zn Across Different Cell Types.

Highest potencies were obtained in TNBC and leukemia cells with low µM IC_{50} values. In prostate cancer lines, intermediate sensitivity was observed. PC-3 cells displayed IC_{50} values of 14.3 µM for Telomir-Zn. LNCaP cells were less sensitive to Telomir-Zn (IC_{50} = 21.3 µM). For both prostate cancer lines, the highest non-toxic concentrations were ~2.5 µM.

Non-malignant control lines were less sensitive to Telomir-Zn whereas HaCaT keratinocytes showed IC_{50} above the tested range. These results indicate strongest cytotoxic effects in hematologic malignancy cells and lower effects in keratinocyte controls within the studied concentration ranges.

In order to elucidate the coupling between Telomir cytotoxicity and Fe^{2+}, MDA-MB-468 (TNBC) cells were co-incubated with Iron (as $FeCl_2$, at 10 µM) and Telomir-Zn at a range of concentrations (0.03–100 µM). Telomir-Zn produced dose-dependent effects on viability, with concentrations at 1µM and higher severely reducing viability, and lower concentrations largely preserving it. Co-incubation with $FeCl_2$, led to a shift to higher concentrations for toxic effect. $FeCl_2$ preserved viability at 1 µM Telomir-Zn, and significantly reduced toxicity at 3 µM of Telomir-Zn. At concentration at and above 10 µM, no more protection was observed (Figure 7). These results show a strong link between Telomir cytotoxicity and Fe^{2+} concentration. Similar protection by iron was present in other studied TNBC cells (data not shown).

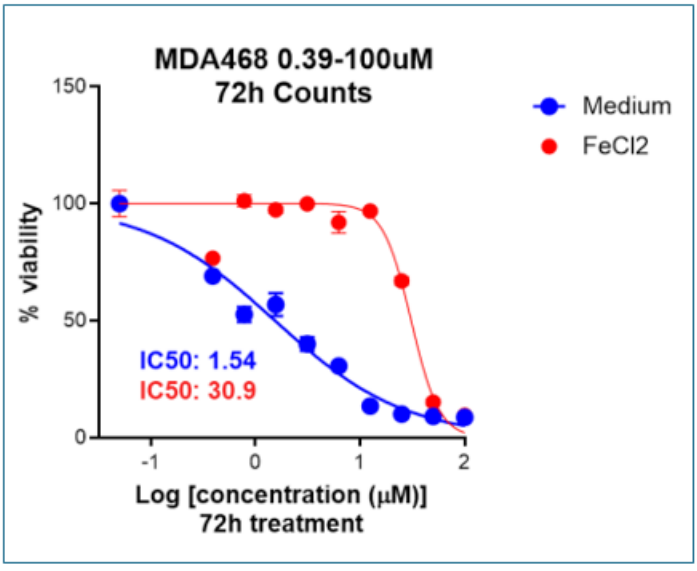

Figure 7: Effect of Telomir-Zn on Viability in MDA-MB-468 Cells in the Absence or Presence of $FeCl_2$ (10 µM). Data represents mean of three replicate measures.

Telomir-Zn Inhibits Fe^{2+}-Dependent Jumonji Histone Demethylases

Histone demethylases (HDMs) of the Jumonji C (JmjC) family constitute a major class of Fe^{2+}-dependent epigenetic regulators frequently dysregulated in cancer. Members of the KDM2, KDM5, and KDM6 families are often overexpressed in aggressive tumors, where they modulate chromatin accessibility and drive transcriptional programs associated with stemness, epithelial-mesenchymal transition (EMT), invasion, and therapeutic resistance.

We have evaluated the direct effects of Telomir-Zn on several representative enzymes of this family.

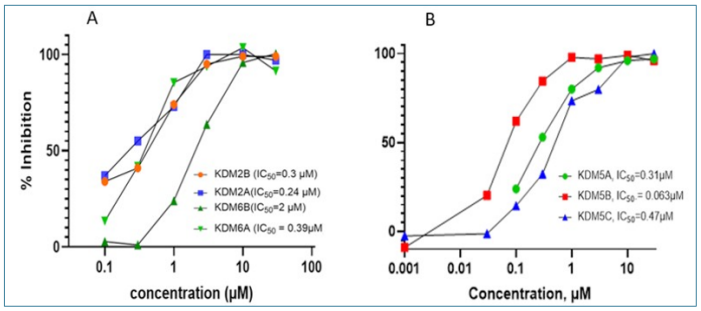

Figure 8: Effect of Telomir-Zn on KDMs. A. KDM2 and KDM6. B. KDM5. Results are means from duplicate measures.

Telomir-Zn inhibited multiple Fe^{2+}-dependent histone demethylases, a class of epigenetic enzymes that regulate chromatin structure, DNA methylation, transcription, and cellular identity. Dysregulation of these enzymes contributes to cancer progression, neurodegeneration, metabolic dysfunction, inflammation, and aging. Within the KDM2 family, Telomir-Zn inhibited FBXL10 (KDM2B) and FBXL11 (KDM2A). KDM2B is frequently overactive in aggressive cancers, where it supports stem-like properties associated with relapse and treatment resistance. KDM2A is elevated in several malignancies and contributes to tumor growth and immune evasion.

Telomir-Zn also inhibited key members of the KDM6 family, including UTX (KDM6A) and JMJD3 (KDM6B). UTX functions as a demethylase that removes repressive histone marks and modulates transcriptional programs relevant to development and cancer. JMJD3 is a major regulator of inflammation and tumor progression; by altering histone modifications linked to DNA methylation, JMJD3 promotes metastasis and facilitates immune escape.

In addition, Telomir-Zn inhibited histone demethylases of the KDM5 (JARID1) family, which specifically remove H3K4me3 and H3K4me2, histone marks associated with active transcription. JARID1A (KDM5A) contributes to tumorigenesis and cancer stem-cell phenotypes; its inhibition increases H3K4me3 at tumor-suppressor gene promoters, enhancing their expression and potentially improving sensitivity to DNA-damaging therapies. JARID1B (KDM5B) is overexpressed in several cancers, where it maintains cancer stem-cell populations and drives drug resistance. Inhibition of KDM5B reduces cell viability, induces cell-cycle arrest, enhances tumor-suppressor gene expression, and impairs DNA-damage repair. JARID1C (KDM5C) regulates genomic stability through control of heterochromatin structure and repression of non-coding RNAs; its loss leads to heterochromatin defects, satellite repeat misexpression, and increased cancer susceptibility.

Oral Telomir-Zn Suppresses Tumor Growth in PC-3 Xenografts

The purpose of this study was to evaluate the anti-cancer efficacy of Telomir-Zn, administered orally, in reducing aggressive human prostate (PC-3) tumor growth in xenograft models and analyzing its effects on telomere length and on DNA methylation of several key proteins. The principle of the study is based on PC-3 derived human prostate tumor model in athymic nude mice imitates human prostate cancer in its progression. Tumor progression can be thereby monitored effectively in live animals, as the tumor interacts with various immune cells and fibroblasts, and therefore, live mice models are essential for evaluating the efficacy of new anti-cancerous drugs like Telomir-Zn. A total of 84 athymic nude mice were utilized and divided into six groups of fourteen animals in each group (10+4 satellite). Four animals treated by PTX 20 mg/kg were found in moribund conditions eleven days following treatment initiation. One animal treated by Telomir-Zn 100 mg/kg was found dead in cage four days following treatment initiation. No mortality was observed with the other treatment groups.

Body weights percentage from Day 1 (treatments initiation) were calculated and statistical analysis was conducted between groups using Prism: One-Way ANOVA followed by Tukey's post-hoc test. No significant differences to controls were observed across the Telomir-Zn treatment groups. As of eight days after the start of treatment administration, it was observed that the group treated by PTX monotherapy showed a statistically significant decrease in average body weight change, and it was statistically significant at day 11 compared to controls. Combination of Telomir-Zn 10 mg/kg and PTX 20mg/kg attenuated the animal's weight loss compared to animals treated by PTX monotherapy, with no statistically significant difference in the average body weight change compared to the groups treated by Telomir-Zn alone or to vehicle. By the end of the treatment period, both PTX and Rapamycin showed some increases in BW, compared to controls (data not shown).

Tumor measurements starting from Day 1 (treatments initiation) were calculated and are presented in Figure 9. Statistical analysis was conducted between groups using Prism: One-Way ANOVA followed by Tukey's post-hoc test. The results showed that the group of animals treated by PTX and Rapamycin showed statistically significantly smaller average tumor volume compared to the group of animals treated by vehicle following eight days of treatment and until the end of the study. Starting from Day 10, of treatment the group of animals treated by the low dose of Telomir-Zn also showed statistically significant smaller average tumor size compared to the vehicle group. The group of animals treated by the high dose of Telomir-Zn exhibited a statistically significant result as of Days 15 of the study. The group of animals treated by the combination of Telomir-Zn10mg/kg and PTX displayed statistically significant smaller average tumor size compared to the vehicle group from Day 10, with no significant differences compared to PTX monotherapy (Figure 9).

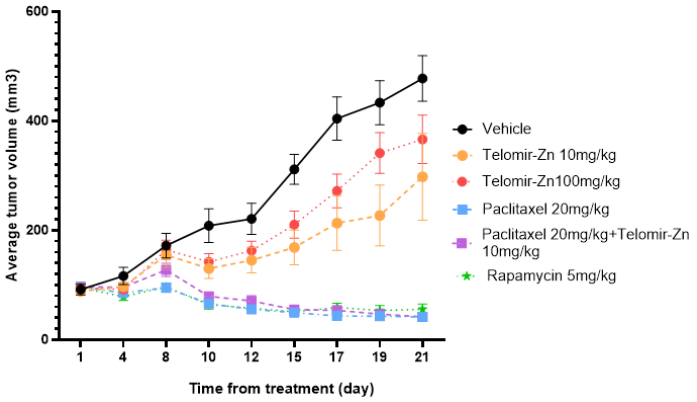

Figure 9: Tumor Volume Measurements.

Mice were injected with $1x10^6$ PC-3 cells subcutaneously into the right flank region of each mouse, and when the tumors volume reached around 100 mm^3, the mice were allocated to groups and began receiving treatment (day 1) and treatment with the indicated groups were initiated.

Tumors were measured every other day for length (L) and width (W) using a digital caliper starting from tumor appearance. Tumor volume (in mm3) was calculated according to the equation (Length × $Width^2$ ×0.5). **Data represent mean ± SEM of 9–10 mice per group.**

In Vivo Evaluation in Zebrafish Tumor Xenografts

To determine whether the in vitro observations translate to an in vivo setting, the antitumor activity of Telomir-Zn was evaluated using zebrafish tumor xenograft models. HCC1806 cells demonstrated robust engraftment and metastatic capacity in zebrafish embryos, confirming the suitability of this model for therapeutic evaluation.

Approximately 49% of implanted tumors persisted after 3 days, with an average of ~8.5 disseminated tumor cells detected in the caudal venous plexus (CVP).

BT-549 Cells

Treatment with Telomir-Zn (1–10 µM) significantly reduced primary tumor size in BT-549 zebrafish xenografts. The magnitude of tumor regression was comparable to that observed with paclitaxel treatment. Combination therapy with paclitaxel and Telomir-Zn produced a significantly greater reduction in tumor size than either monotherapy, indicating a positive pharmacological interaction. However, none of the treatments significantly affected metastatic dissemination in this model (Figure 10).

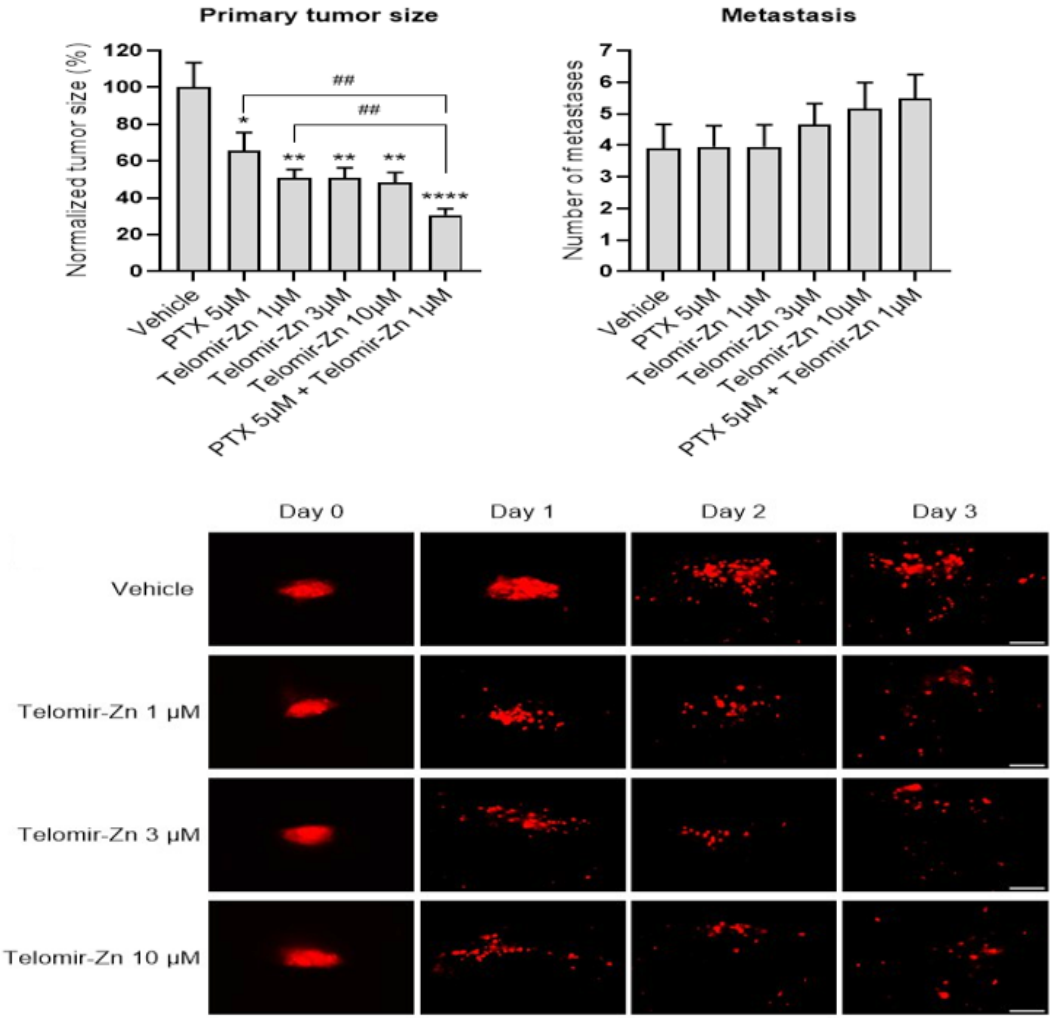

Figure 10: Antitumor efficacy of paclitaxel and Telomir-Zn in BT-549 zebrafish xenografts.

Primary tumor size and metastatic dissemination were evaluated in BT-549 xenografts after 3 days of treatment. Data are normalized relative to the negative control group and presented as mean ± SEM. Statistical significance was determined using one-way ANOVA ($p < 0.0001$) followed by a two-tailed Student's t-test. *$p<0.05$, **$p<0.01$, ***$p<0.0001$ indicate significance compared with the vehicle group; ##$p < 0.01$ indicates significance compared with the respective monotherapies.

HCC1806 Xenografts

In HCC1806 xenografts, Telomir-Zn demonstrated concentration-dependent antitumor activity. Significant reductions in primary tumor size were observed at concentrations of 3 μM and 10 μM. Combination treatment with paclitaxel and Telomir-Zn resulted in a greater reduction in tumor size than either treatment alone.

Importantly, treatment with Telomir-Zn at 3 μM also significantly reduced metastatic dissemination to the caudal venous plexus (CVP), suggesting a potential anti-metastatic effect (Figure 11).

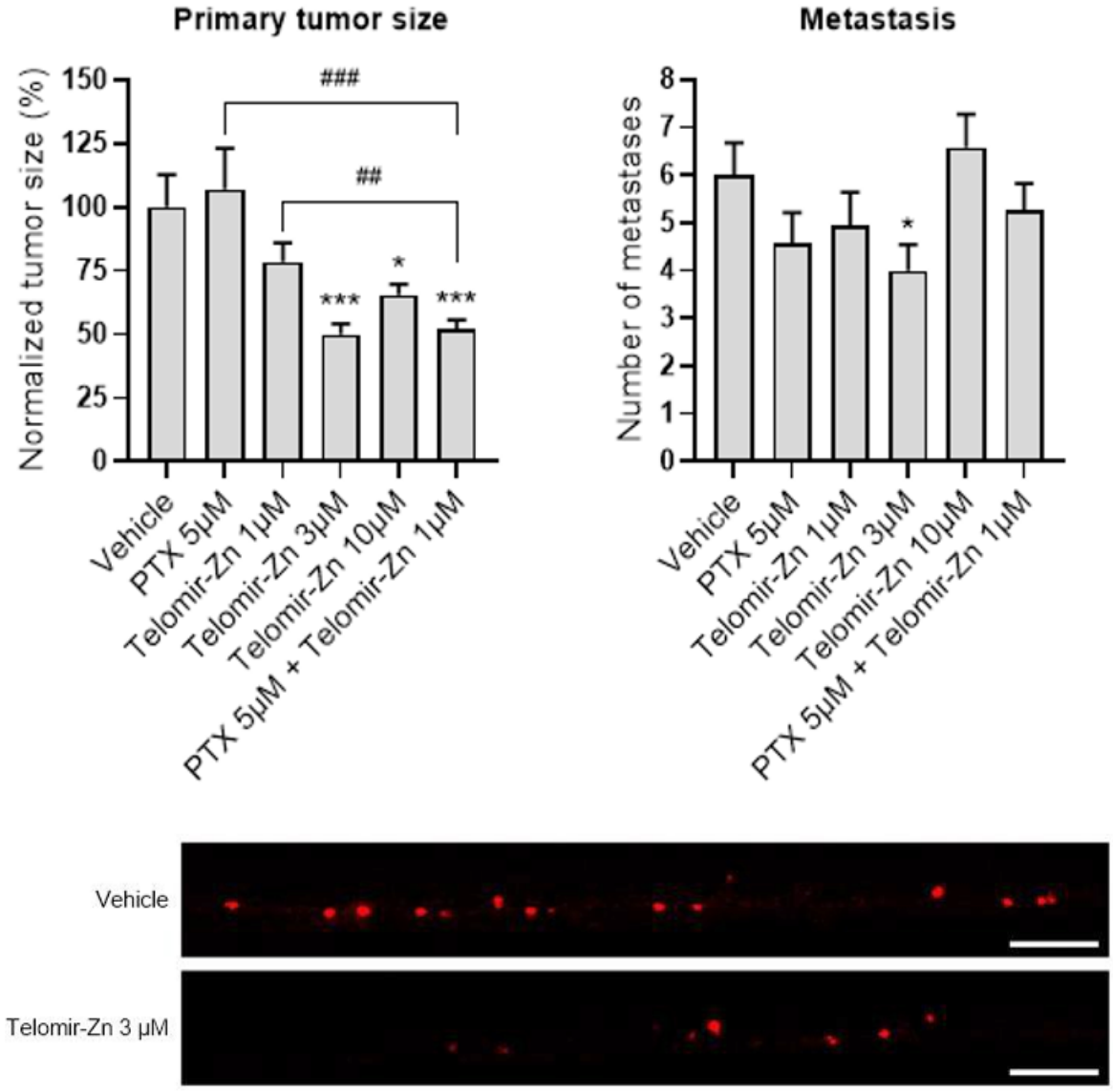

Figure 11: Antitumor efficacy of paclitaxel and Telomir-Zn in HCC1806 zebrafish xenografts.

Primary tumor size and metastatic dissemination were evaluated in HCC1806 xenografts after 3 days of treatment. Data are normalized relative to the negative control group and presented as mean ± SEM.

Normality was assessed using the D'Agostino–Pearson test. For primary tumor size, statistical significance was evaluated using the Kruskal–Wallis test ($p < 0.0001$), followed by the Mann–Whitney test. $p < 0.05$ and $^{**}p < 0.001$ indicate significance compared with the vehicle group; $^{\#\#}p < 0.01$ and $^{\#\#\#}p < 0.001$ indicate significance compared with the respective monotherapies.

For metastasis data, statistical analysis was performed using one-way ANOVA ($p = 0.0617$), followed by a two-tailed Student's *t*-test. $p < 0.05$ indicates significance compared with the vehicle group.

MDA-MB-231 Xenografts

In contrast to the other models, MDA-MB-231 xenografts did not respond to Telomir-Zn, paclitaxel, or their combination. Neither tumor growth nor metastatic dissemination differed significantly from vehicle-treated controls. These findings suggest the presence of intrinsic resistance mechanisms in certain TNBC subtypes (data not shown).

Telomere Length Analysis

Telomere length was quantified in tumor tissues at multiple time points, with results from two time points shown in Figure 12. Statistical comparisons among treatment groups were performed using one-way ANOVA followed by Tukey's post-hoc test.

On Day 10, no significant differences in telomere length were detected between any treatment group and the vehicle, although some increase was noted with the PTX group. No major differences in telomer lengths were observed in vehicle group, when day 10 was compared with day 21. By Day 21, Telomir-Zn at both doses did not alter telomere length relative to the vehicle. In contrast, paclitaxel, rapamycin, and the combination of Telomir-Zn (low dose) with paclitaxel were associated with statistically significant increased telomere length at this time point (Figure 12).

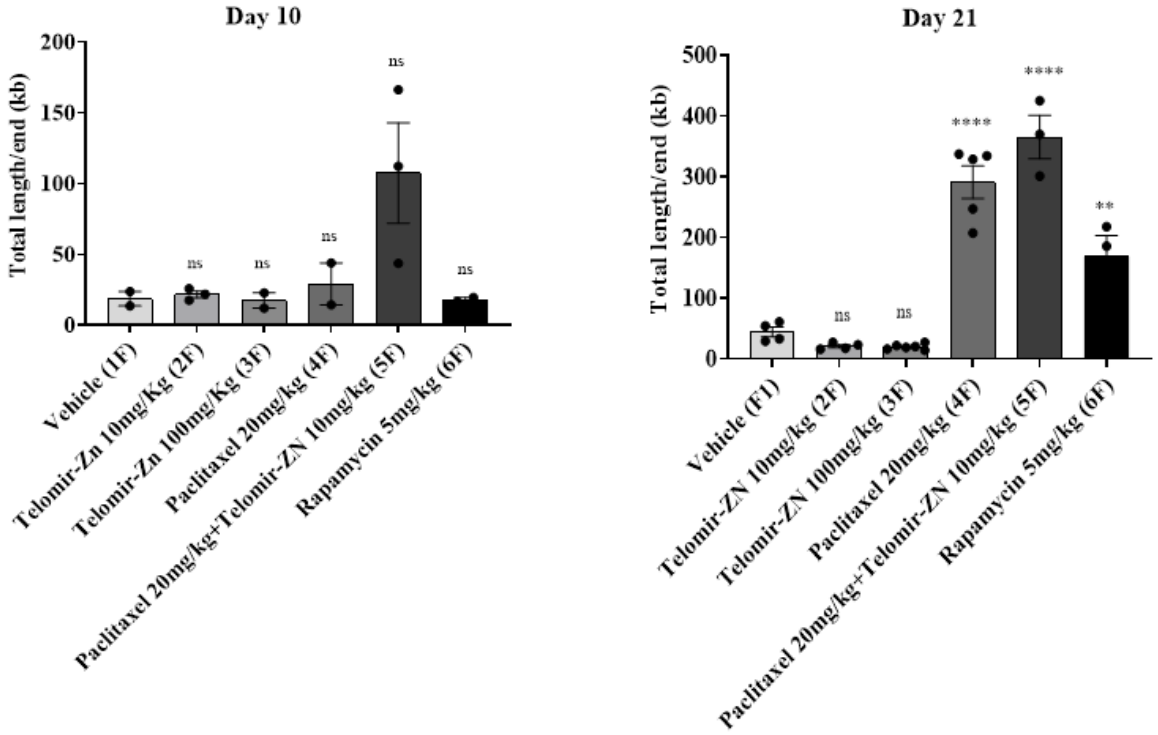

Figure 12: Telomere Length Determined by qPCR.

Relative telomere length was measured by quantitative PCR using telomeric repeat primers and normalized to a single-copy reference gene. DNA was isolated from tumor tissues collected on Day 10 (A) and at study termination on Day 21 (B). **Data represent mean ± SEM of 4–7 tumor DNA samples per group.** Statistical comparisons among treatment groups were performed using one-way ANOVA with Tukey's post hoc test (**p < 0.01; ****p < 0.0001; ns = not significant).

DNA Methylation Analysis

DNA methylation levels of selected tumor-regulatory genes were quantified in tumor tissues at multiple time points to assess potential epigenetic alterations associated with tumor progression and treatment response (Figure 13). Statistical comparisons among treatment groups were performed using one-way ANOVA with Tukey's post hoc test (*p < 0.05; **p < 0.01; ***p < 0.001; ns = not significant).

The analyzed genes play key roles in tumor suppression and apoptotic regulation. STAT1 promotes cell-cycle arrest and apoptosis; TMS1 (PYCARD/ASC) regulates programmed cell death; CDKN2A encodes p16^INK4A and p14^ARF, which control cell-cycle progression; GSTP1 detoxifies carcinogens and limits oxidative DNA damage; RASSF1A regulates mitotic progression and apoptosis; MASPIN (SERPINB5) inhibits invasion and metastasis; and CASP8 mediates death-receptor–dependent apoptosis.

When methylation levels were compared across time points (pre-inclusion, Vehicle Day 10, and Vehicle Day 21), most genes showed progressive hypermethylation in the vehicle group, with the exception of STAT1 and CASP8. This increase in methylation is consistent with transcriptional silencing of tumor-suppressor pathways and may account for the tumor progression observed in untreated animals [19].

By Day 21, Telomir-Zn 100 mg/kg reduced methylation levels across most genes relative to the vehicle, with the exception of TMS1. Comparison of the two Telomir-Zn doses indicated a dose-dependent reduction in methylation for several genes, excluding STAT1 and CASP8. Rapamycin, used as a positive control, induced significant demethylation across multiple genes. Paclitaxel demonstrated limited demethylating activity, with reductions observed only in TMS1 and RASSF1A. The combination of Telomir-Zn 10 mg/kg with Paclitaxel significantly reduced methylation of STAT1, TMS1, and RASSF1A compared with the vehicle, with non-significant trends toward reduced methylation in GSTP1, MASPIN, and CASP8 (Figure 13).

Collectively, these results indicate that Telomir-Zn reduces promoter hypermethylation in the majority of the key tumor-suppressor genes studied in vivo. Although the dose–response relationship was not uniform across all targets, both Telomir-Zn doses produced meaningful DNA demethylating reduction effects relative to the vehicle. These findings support an epigenetic mechanism through which Telomir-Zn may contribute to tumor suppression.

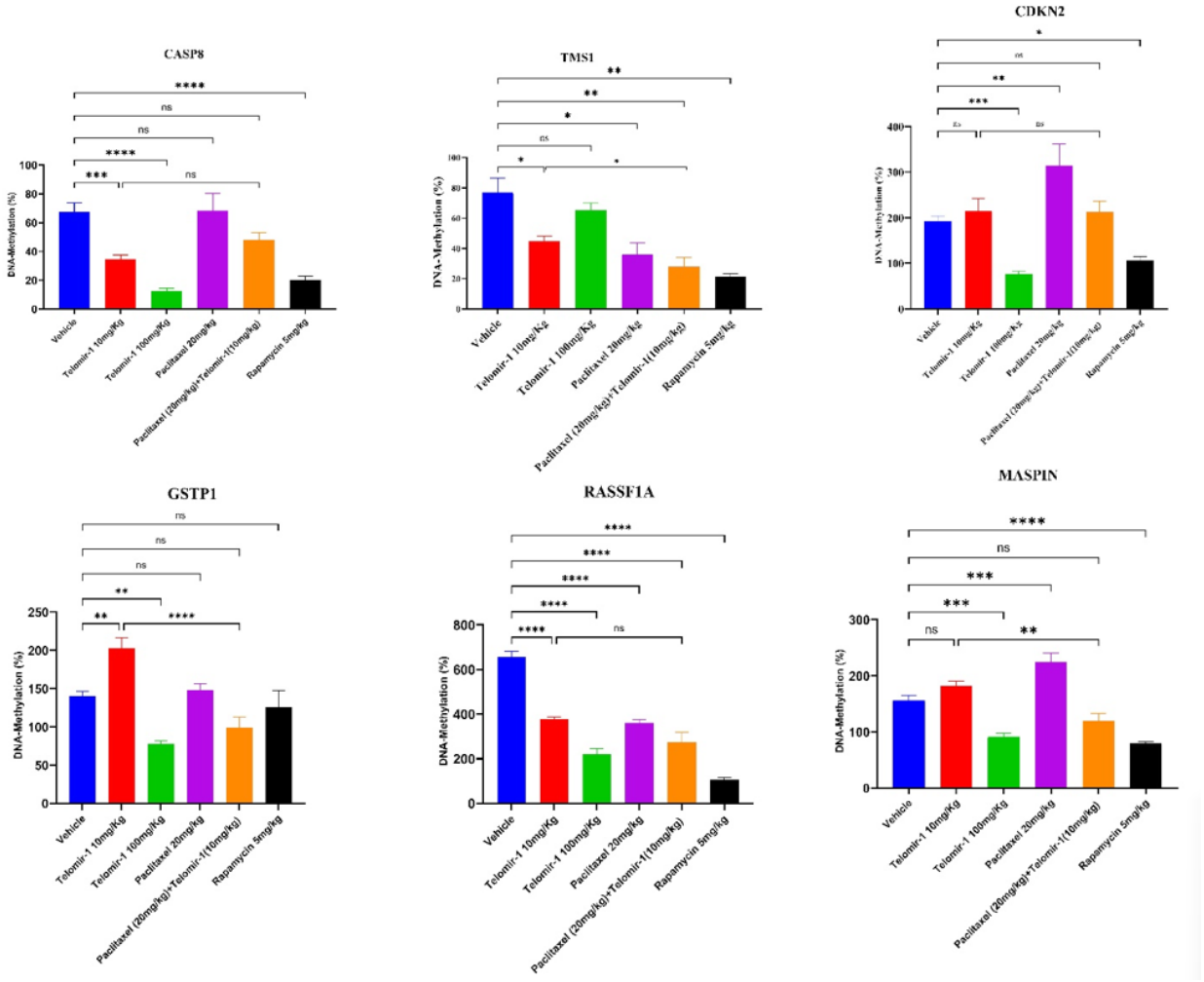

Figure 13: DNA Methylation Levels in Tumor Tissue.

Methylation levels are presented as the percentage of the amplified genomic region following treatment. Groups are marked as following: 1F- Vehicle control, 2F – Telomir-Zn, 10 mg/kg; 3F- Telomir-Zn, 100 mg/kg; 4F- Paclitaxel 20 mg/kg; 5F- Paclitaxel 20 mg/kg + Telomir-Zn, 10 mg/kg; 6F-Rapamycin 5 mg/kg. Levels of CDKN2A are expressed at day 10 (A) and 21 (B); Levels of CASP8 are expressed at day 10 (C) and 21 (D); Levels of GSTP1 are expressed at day 10 (E) and 21 (F); Levels of MASPIN are expressed at day 10 (G) and 21 (H); Levels of RASSF1A are expressed at day 10 (I) and 21 (J); Levels of TMS1 are expressed at day 10 (K) and 21 (L). **Data represent mean ± SEM of 4–9 tumor DNA samples per group.** Statistical comparisons among treatment groups were performed using one-way ANOVA with Tukey's post hoc test (*$p < 0.05$; **$p < 0.01$; ***$p < 0.001$; ****$p < 0.0001$,ns = not significant).

Together, these findings indicate that Telomir-Zn targets multiple epigenetic regulators across the KDM2, KDM5, and KDM6 families, resulting in the accumulation of histone methylation marks associated with transcriptional repression of oncogenic pathways and reactivation of tumor-suppressor programs.

Materials and Methods

Definition and Use of Telomir-Zn

Telomir-Zn (2,4,6-tris(3,4-dihydro-2H-pyrrol-2-yl)pyridine, $ZnCl_2$) refers to the active pharmaceutical ingredient (API), which was used for all assays, chelation studies, and mechanistic evaluations.

Chelation Assay In Vitro

Ferene based measurements of free Fe^{2+} ions in solutions.

Fe^{2+}, Cu^{2+}, Zn^{2+} working solutions at 0.8 mM were freshly prepared from $FeSO_4$, $CuCl_2$ and $ZnCl_2$ (Merck # 12354, #C3279, #793523) in HPLC-grade water (J.T. BAKER #4218-03) and filtered through 0.22 µM PES filters. Telomir-Zn (TEL001UK-3) stock at 20 mM, and DFO (Merck #D9533) stock at 15 mM in HPLC-grade water. Prior to use, all chelators were diluted in ammonium acetate (Merck #A1542) buffer (2.5 M, pH 7.2) to a working concentration of 100 µM, maintaining 1% (v/v) ethanol in all conditions to control for solvent effects. Ferene (Merck #82940) working solution was prepared in assay buffer (pH 7.2) to a final Ferene concentration of 2.8 mM.

An Fe^{2+} standard curve was generated in parallel by serial dilution 1:2 (0-800 µM) and used to convert absorbance values to free Fe^{2+} concentrations. Samples containing Fe^{2+} at a constant initial concentration were incubated with increasing concentrations of Telomir-Zn or DFO for 10 min at room temperature. Ferene solution was then added, followed by an additional 10 min incubation to allow chromophore development. Absorbance was measured at 595 nm using a plate reader, and free Fe^{2+} levels were calculated relative to the standard curve.

For the competition assay stock solution was prepared in assay buffer (pH 7.2) to a final Ferene concentration of 2.8 mM. Stock solutions of Telomir-Zn (20 mM in water), and deferoxamine (DFO; 15 mM in water) were diluted in assay buffer containing 1% EtOH to prepare 400 µM working stocks.

Fifty microliters of each test compound (400 µM) were dispensed into wells of a 96-well polypropylene (PP) plate. $ZnCl_2$ or $CuCl_2$ solutions (50 µL; 12.5–800 µM) were added to the respective wells and incubated for 10 minutes at room temperature to allow metal–compound interaction. Subsequently, 100 µL of $FeSO_4$ solution (200 µM) was added to each well. In parallel, $FeSO_4$ standards (6.25–400 µM) were prepared in the same PP plate.

For quantification of free Fe^{2+}, 100 µL Ferene working solution was added to clear, flat-bottom 96-well plates, followed by transfer of 50 µL from each PP-plate reaction well. After incubation for 10 min at room temperature, absorbance was measured at 595 nm using a microplate reader. Free Fe^{2+} concentrations were calculated from the $FeSO_4$ standard curve.

The Ferene assay generated a concentration-dependent absorbance signal with excellent linearity across the tested range ($R^2 > 0.998$). The lowest concentration evaluated (6 µM) was detectable but produced only a weak signal, whereas absorbance values above 0.1 O.D. were consistently observed at 25 µM and higher. For Fe^{2+} standards prepared from $FeSO_4$, the presence of ascorbic acid did not noticeably affect either signal intensity or linearity.

Fluorescent Measurements

Cell culture and seeding. HaCaT (AddexBio T0020001) keratinocytes were maintained in DMEM (Biowest #L0501) supplemented with 10% fetal bovine serum (FBS) (GIBCO #A5256701), 2 mM sodium pyruvate (Biowest #LO642-100), and 1% penicillin/streptomycin (GIBCO #15140-122). On day 1, cells were seeded into six 96-well plates at a density ensuring subconfluent growth at the time of treatment.

Chelator treatment. On day 2, cells were treated with Telomir-Zn, or DFO at final concentrations ranging from 0.25 to 50 µM. Vehicle controls were included in parallel. Cells were incubated with compounds for 3, 6, or 16 h at 37°C in a humidified incubator with 5% CO_2.

FerroOrange staining. At each time point, treatment medium was removed and cells were washed three times with Hank's Balanced Salt Solution (HBSS). FerroOrange (Dojindo Laboratories # F374) at final concentration 1 µM prepared in HBSS was added to each well, and plates were incubated for 30 min at 37°C to allow probe loading and Fe^{2+}-dependent fluorescence development.

Fluorescence quantification and imaging. Following staining, fluorescence was first quantified in the 96-well format using a CLARIOstar plate reader (BMG Labtech). Wells were subsequently imaged using a fluorescence microscope at 5×, 10× and 20× magnification. Imaging was performed with excitation at 546 nm and emission collected using a band-pass 575–640 nm filter set. Analysis of IC_{50} was performed using the software GraphPad Prism.

Cell Culture, Treatment, and Viability Assays

Human triple-negative breast cancer (TNBC) cell lines MDA-MB-468, HCC70, HCC1806, and BT-549 were obtained from ATCC (American Type Culture Collection, Manassas, VA, USA) and cultured under the supplier's recommended conditions.

PC-3 (ATCC CRL-1435) prostate cancer cells were cultured in F-12K; LNCaP clone FGC (ATCC CRL-1740) prostate cancer cells in RPMI-1640 with 2 mM L-glutamine; HL-60 (ATCC CCL-240) leukemia cells in RPMI with 15% FBS; HaCaT keratinocytes in DMEM with 2 mM sodium pyruvate. Unless otherwise noted,

media were supplemented with 10% FBS and 1% penicillin/streptomycin. All cell lines were maintained at 37°C in 5% CO_2 and passaged routinely to preserve logarithmic growth. On day 1, cells were seeded into 96-well plates at a density chosen to ensure 20-40% confluence at the time of treatment. On day 3, cells were treated with Telomir-Zn at a range of concentrations prepared in the corresponding culture medium. HL-60 cells in suspension were treated on the day of seeding. Vehicle-treated controls were included in parallel. Cells were incubated with compounds for 48 h prior to endpoint analyses. At the end of treatment, cells were visually inspected and imaged by light microscopy to assess morphology, confluency, and gross cytotoxic effects.

At the end of each incubation period, representative images of all treatments were captured. After imaging, the medium was discarded and replaced with 100 µL of fresh medium.

Cell numbers were calculated from a standard curve generated using untreated cells seeded at known densities under identical assay conditions. Concentration–response relationships were fitted by nonlinear regression in GraphPad Prism to obtain IC_{50} values. Experiments included technical replicates, and viability was normalized to vehicle controls. Because viability did not reach zero at any tested dose, curve fitting used a fixed theoretical upper concentration of 1000 µM.

Histone Demethylase (KDMs) Assay

Evaluation of the effects of Telomir-Zn on KDMs activities were conducted as previously described (26-27). These assays consist on studying in Sf9 human recombinant cells, expressing the respective enzyme, using as substrates Biotin-H3K4me2, Biotin-H3K27me2 or Biotin-H3K36me1 for KDM5s, KDM6s and KDM2s, respectively.

In Vivo Studies

The mouse is a commonly used species for cancer studies for evaluating the efficacy of new anti-cancerous drugs in accordance with international recommendations and the published literature. The Athymic Nude strain is a well-known laboratory model with sufficient historical data of developing PC-3–derived prostate tumors.

Animals handling was performed according to guidelines of the National Institute of Health (NIH) and the Association for Assessment and Accreditation of Laboratory Animal Care (AAALAC). For this study, mice were housed in individual cages separately (up to 5 per cage) measuring 36.5 x 20.7 x 13 cm with stainless steel top grill facilitating pelleted food and drinking water in plastic bottle; bedding: steam sterilized clean paddy husk (Envigo, Teklad, Laboratory grade, Sani-chips). Bedding material was changed along with the cage at least twice a week. This study was performed in compliance with "The Israel Animal Welfare Act" and following "The Israel Board for Animal Experiments" Ethics Committee approval # NPC-Ph - IL - 2412 – 524.

PC-3 cell injection was performed under inhalational isoflurane anesthesia (3%). A total of 84 mice were utilized and divided into six groups of fourteen animals in each group (10+4 satellite). The number of groups and the total number of animals was based on previous studies and specific guidelines demonstrating that this was the minimum number of animals sufficient to obtain indicative/significant information. Animals were randomized to treatment groups based on tumor volume prior to dosing. Tumor measurements were performed in a blinded manner.

Animals were fed ad libitum a commercial rodent diet (Teklad Certified Global 18% Protein Diet, Envigo cat# 2018SC). Animals had free access to sterilized and acidified drinking water (pH between 2.5 and 3.5) obtained from the municipality supply and treated according to Pharmaseed's SOP No. 214: 'Water system".

Animals were housed under standard laboratory conditions, air conditioned and filtered (HEPA F6/6) with adequate fresh air supply (Minimum 15 air changes/hour). Animals were kept in a climate-controlled environment. Temperatures range was 19–26°C and relative humidity range 35–70% with a 12-hours light and 12-hours dark cycle (6AM/6PM).

Allocation to treatment groups was carried out 10 days post cells injection based on tumors growth to achieve as much as possible balanced groups. The study was conducted in one cycle. Mice were injected with $1x10^6$ PC-3 cells subcutaneously into the right flank region of each mouse, and when the tumors volume reached around 100 mm^3, the mice were allocated to groups and began receiving treatment. Six mice (satellites) were sacrificed at this point. Following 12 days of treatment, additional three mice from each group (the satellites) were sacrificed and tumors were collected. Study ended on Day 21 post treatment and tumors were collected from all mice. Animal received vehicle (40% HPβCD+5% DMSO in water), 10 or 100 mg/kg orally at 7.5 mL/kg; PTX (without or with 10 mg/kg of Telomir-Zn) at 20 mg/kg at 10 or 7.5 mL/kg Ip or Po, respectively; or rapamycin at 5 mg/kg at 7.5 mL/kg PO.

Tumors were measured every other day for length (L) and width (W) using a digital caliper starting from tumor appearance. Tumor volume (in mm3) was calculated according to the equation (Length × $Width^2$ ×0.5).

At study termination, animals were euthanized using CO_2 inhalation in accordance with approved protocols.

Zebrafish Xenografts

Transgenic Tg(fli1:EGFP)y1 zebrafish embryos were raised at 28 °C for 48 h in E3 embryo medium supplemented with 0.2 mM 1-phenyl-2-thiourea (PTU). Unfertilized eggs or larvae that appeared unhealthy or exhibited developmental defects were

excluded prior to the start of the experiment.

Cancer cells were labeled with the red fluorescent dye DiI. Approximately 500–700 labeled cancer cells were subcutaneously implanted into the perivitelline space of 2-day-old embryos. Embryos in which tumor cells were inadvertently injected into the circulation or incorrectly implanted in the yolk rather than the perivitelline space were excluded from the study.

Selected tumor-bearing embryos were sorted into experimental groups (50 embryos per group), and images of primary tumors were acquired immediately after tumor implantation. Tumor-bearing embryos were incubated in E3/PTU medium in the presence of paclitaxel and Telomir-Zn for 3 days at 35.5 °C, with treatment renewed daily.

After the incubation period, images of primary tumors and tails were captured using a red fluorescent filter. Embryos that died or were otherwise lost during the study were excluded from the final analysis.

Images obtained immediately after implantation (day 0) and after 72 h of incubation (day 3) were analyzed using in-house developed software. Primary tumor regression was calculated and normalized to the negative treatment group. The number of disseminated tumor cells in the caudal venous plexus (CVP) after 3 days was manually counted.

Telomere Length Analysis

Absolute human telomere length analysis from tumor tissue of sacrificed satellite mice at 10- and 21-days timeline was determined by using: Absolute Human Telomere Length Quantification qPCR Assay Kit according to the manufacturers kit protocol. ScienCell's Absolute Human Telomere Length Quantification qPCR Assay Kit is designed to directly measure the average telomere length of a human cell population. The telomere primer set recognizes and amplifies telomere sequences. The single copy reference (SCR) primer set recognizes and amplifies a 100 bp-long region on human chromosome 10 and serves as a reference for data normalization. The reference genomic DNA sample with known telomere length serves as a reference for calculating the telomere length of target samples. The carefully designed primers ensure: (i) high efficiency for trustworthy quantification; and (ii) no non-specific amplification. Each primer set has been validated by qPCR with melt curve analysis for amplification specificity and by template serial dilution for amplification efficiency.

DNA Methylation Analysis

Human quantification of DNA methylation analysis from tumor tissue of sacrificed satellite mice at 10 and 21 days was determined using: OneStep PLUS qMethyl™ Kit according to the manufacturers kit protocol. The OneStep PLUS qMethyl™ PCR Kit was intended for the quantification of human DNA methylation at custom-selected genomic regions. The same DNA sample was analyzed in parallel with the Test PreMix and the Reference PreMix. The Test PreMix contains enzymes that selectively digest unmethylated DNA while leaving methylated DNA intact. Only methylated DNA were amplified in the "Test Reaction." The Reference PreMix does not contain those enzymes, therefore both methylated and unmethylated DNA are amplified in the "Reference Reaction." The difference in Cycle threshold (Ct) values between the Reference and Test reactions was used to calculate the percentage of DNA methylation at the selected genomic region. Data represent mean ± SEM of 4–9 tumor DNA samples per group. While initially 10 mice were studied per group, not all tumor samples were sufficiently large to extract the DNA and the number of samples are therefore variable.

Statistical Analysis

Data are presented as mean ± standard error of the mean (SEM) unless otherwise indicated. For Mice studies, group comparisons were performed using one-way ANOVA followed by Tukey's post hoc test for multiple comparisons. For tumor volume, telomere length, and DNA methylation analyses, treatment groups (vehicle, Telomir-Zn 10 mg/kg, Telomir-Zn 100 mg/kg, paclitaxel, Telomir-Zn + paclitaxel, and rapamycin) were compared at the indicated time points. Statistical analyses were performed using GraphPad Prism (version 10.5.0; GraphPad Software, San Diego, CA).

For Zebrafish studies, normality testing was performed prior to statistical analysis, followed by appropriate parametric or non-parametric tests, including one-way ANOVA or Kruskal–Wallis tests, followed by two-tailed Student's t-test or Mann–Whitney tests where specified.

Discussion

Telomir-Zn represents a mechanistically differentiated approach that exploits convergent vulnerabilities in iron metabolism and epigenetic regulation. By rapidly depleting labile Fe^{2+} and inhibiting multiple JmjC histone demethylases, it promotes accumulation of activating histone marks, antagonizes DNA methylation at tumor-suppressor promoters, and induces growth arrest or death preferentially in iron-addicted cancer cells.

The iron-rescue data in TNBC lines and the observed promoter demethylation in prostate tumors provide orthogonal evidence linking metal modulation to epigenetic reprogramming. Heterogeneous responses across TNBC models and the stronger anti-metastatic effect in HCC1806 highlight the importance of tumor-specific metabolic and epigenetic context, supporting biomarker-driven patient stratification based on labile iron pools, KDM expression, or iron-handling gene signatures.

Iron chelation is a known therapeutic strategy, with deferoxamine (DFO) as a benchmark due to its high iron affinity [25, 28, 29]. This study shows that Telomir-Zn acts as metal-dependent epigenetic modulator distinct from DFO. While DFO has high Fe^{2+} affinity, Telomir compounds show moderate Fe^{2+} affinity, preferential Cu^{2+} binding, and minimal Zn^{2+} interaction. This suggests they function as redox-metal modulators rather than strict chelators.

Despite lower Fe^{2+} affinity, Telomir-Zn depletes intracellular Fe^{2+} more rapidly, highlighting the importance of cellular permeability. Unlike DFO, Telomir compounds engage intracellular Fe^{2+} quickly, aligning with their early FerroOrange kinetics. Effective intracellular modulation thus depends on accessibility, not just binding strength.

Their rapid Fe^{2+} depletion led to selective cytotoxicity in iron-dependent malignancies, with iron-rescue experiments confirming Fe^{2+} depletion as the antiproliferative driver. In this context, iron-dependent tumors are those with elevated labile iron and reliance on Fe^{2+}-dependent enzymes. In vivo, oral Telomir-Zn suppressed PC-3 tumor growth with favorable tolerability, consistent with a progressive epigenetic reprogramming mechanism. Importantly, telomere length was unaffected, suggesting no telomerase or replicative stress involvement.

Copper's role in oncogenesis [8, 30] further supports Telomir-Zn's dual Fe/Cu targeting, which may be advantageous in cancers where both metals play a role. A key finding is Telomir-Zn's reduction of promoter hypermethylation in tumor-suppressor genes, aligning with inhibition of Fe^{2+}-dependent Jumonji C demethylases. By limiting Fe^{2+} availability, Telomir-Zn reprograms epigenetics without broad chromatin disruption, unlike DNMT or HDAC inhibitors.

Intracellular iron concentrations are substantially higher than those of copper, with iron present in micromolar pools (including both labile and protein-bound fractions), whereas copper is maintained at much lower, tightly regulated levels due to its high redox reactivity [31, 32]. These quantitative differences are critical for interpreting the dual metal-modulating properties of Telomir [33, 34]. In this context, we believe that the biological impact of Telomir is not solely determined by total metal abundance but rather by its interaction with the labile, bioactive metal pools that regulate enzymatic activity and redox signaling. While iron modulation is likely the dominant driver of effects on Fe^{2+}-dependent enzymes such as JmjC histone demethylases, even small perturbations in labile copper can have disproportionate effects on redox balance, mitochondrial function, and copper-dependent enzymes due to the tight homeostatic control of this metal. Thus, the apparent dual activity of Telomir may reflect differential but complementary modulation of iron- and copper-dependent pathways, rather than equivalent quantitative targeting of both metals.

The present study demonstrates that Telomir-Zn exerts antitumor activity across multiple TNBC and other cancer models, with heterogeneous responses observed between cell lines. The most direct mechanistic observation in this dataset is the rescue of Telomir-Zn cytotoxicity following Fe^{2+} supplementation, suggesting an iron-dependent component of the compound's activity.

The observed reduction in promoter DNA methylation following Telomir treatment is mechanistically consistent with inhibition of Fe^{2+}-dependent Jumonji C histone demethylases (KDMs). These enzymes regulate key histone methylation marks that control chromatin accessibility and transcriptional activity [35, 36]. Depletion of intracellular labile Fe^{2+} impairs KDM catalytic function, leading to accumulation of activating histone marks such as H3K4me3 and H3K36me2. These chromatin changes are known to antagonize DNA methylation by limiting recruitment and activity of DNA methyltransferases (DNMTs), which preferentially target transcriptionally repressed and H3K4-unmethylated regions. In parallel, the establishment of a more permissive chromatin environment promotes transcriptional activation and facilitates passive and active DNA demethylation processes, including reduced maintenance methylation during replication and enhanced accessibility to TET-mediated oxidation pathways [37, 38]. Consistent with this framework, Telomir treatment resulted in decreased promoter methylation across multiple tumor suppressor genes, including STAT1, GSTP1, RASSF1A, CDKN2A, and MASPIN. These findings support a model in which modulation of intracellular metal availability induces coordinated epigenetic reprogramming, linking metabolic control of Fe^{2+}-dependent enzymes to both histone and DNA methylation landscapes. Unlike direct DNMT inhibitors, this mechanism enables simultaneous regulation of multiple chromatin-modifying pathways, providing a broader and potentially more physiologic strategy to reverse epigenetic silencing in iron-dependent malignancies.

However, given the central roles of iron and copper in redox biology and cellular metabolism, these effects are unlikely to be exclusively epigenetic. Modulation of labile Fe^{2+} and Cu^{2+} pools can alter reactive oxygen species dynamics, mitochondrial function, and metal-dependent enzymatic processes, all of which may contribute to the observed anti-tumor activity. The partial rescue of cytotoxicity by exogenous iron further supports a broader dependence on metal availability that integrates metabolic and epigenetic vulnerabilities. Together, these findings support a model in which Telomir induces coordinated epigenetic reprogramming in parallel with redox and metabolic modulation, with these processes acting in an interconnected manner rather than as independent mechanisms.

The zebrafish xenograft experiments further support the

translational potential of Telomir-Zn by demonstrating antitumor activity in vivo. Zebrafish xenograft models have emerged as powerful preclinical tools capable of rapidly evaluating therapeutic response and metastatic dissemination [39, 40].

The enhanced activity observed in combination with paclitaxel suggests that modulation of metal homeostasis may sensitize tumors to cytotoxic chemotherapy. Future studies should investigate whether Telomir-Zn influences oxidative stress pathways, ferroptosis susceptibility, or iron-dependent chromatin regulation [41-43].

This study further indicates that Telomir-Zn elicits a heterogeneous but biologically coherent antitumor response across breast cancer xenograft models, driven by cell line–dependent molecular vulnerabilities rather than uniform cytotoxicity. Sensitivity to Telomir-Zn in HCC1806 and BT-549 xenografts may be associated with dysregulated iron handling, characterized by elevated labile Fe^{2+} pools, limited ferritin buffering capacity, and increased basal oxidative stress, which together may confer susceptibility to redox imbalance induced by iron and copper chelation.

In these models, disruption of Fe^{2+}-dependent JmjC histone demethylases may further compromise epigenetic plasticity, leading to transcriptional instability, replication stress, and growth arrest or cell death, with a potential contribution of ferroptotic mechanisms in BT-549. In contrast, MDA-MB-231 xenografts may exhibit resistance due to enhanced antioxidant buffering, adaptive metabolic programs, and compensatory signaling networks, including KRAS–STAT3 pathways, which together may limit sensitivity to metal-dependent therapeutic stress [7, 44, 45].

The current in vivo study in mice was conducted in athymic nude mice, which lack functional T cells and therefore do not fully capture the eventual contribution of adaptive immunity to tumor progression and therapeutic response. This limitation is particularly relevant in the context of metal biology, as iron and copper homeostasis are closely linked to immune cell function, inflammatory signaling, and tumor–immune interactions. Modulation of labile Fe^{2+} and Cu^{2+} may therefore influence not only tumor cell–intrinsic pathways but also components of the tumor microenvironment, including innate and adaptive immune responses, which are not represented in this model [46-48]. The data of TNBC cells in zebrafish, an established in vivo system that enables interrogation of whole-organism redox biology, metal homeostasis, and immune–metabolic interactions. Telomir-Zn significantly reduced primary tumor size in BT-549 and HCC1806 xenografts and decreased metastatic dissemination in HCC1806. These findings support a broader, systemic effect of metal modulation consistent with the mechanisms described here, although the translational relevance to mammalian tumor–immune interactions remain to be fully defined. Accordingly, the anti-tumor effects observed in the current mice study should be interpreted primarily as tumor cell–autonomous, and further evaluation in immunocompetent and syngeneic mammalian models will be required to delineate the contribution of immune-mediated mechanisms and their potential therapeutic implications.

Emerging evidence supports the concept of iron addiction, whereby subsets of cancers, including TNBC, reprogram iron metabolism to increase iron uptake, retain intracellular iron, and expand the labile iron pool in order to sustain proliferation, redox balance, and epigenetic plasticity. In the literature, this phenotype is generally inferred from a combination of features rather than a single marker, including increased CD71 expression, reduced ferroportin-mediated iron export, higher intracellular labile iron, and preferential sensitivity to iron depletion or chelation [49-51]. In this context, inhibition of Fe^{2+}-dependent JmjC histone demethylases represents a plausible downstream vulnerability, disrupting chromatin dynamics and contributing to transcriptional instability, replication stress, and growth arrest or cell death. These effects may be amplified in more iron-dependent tumors and, in some settings, may intersect with ferroptotic vulnerability. In contrast, less sensitive models such as prostate or pancreatic cells may show relative resistance through lower reliance on labile iron, stronger antioxidant buffering, greater metabolic adaptability, or compensatory signaling pathways.

The preferential affinity of Telomir-Zn for Cu^{2+} over Fe^{2+} is particularly relevant in TNBC, where copper plays a critical role in metastatic progression. Beyond its well-established functions in mitochondrial energy metabolism, copper drives multiple steps of the metastatic cascade, including extracellular matrix remodeling via LOX, modulation of the pre-metastatic niche, and maintenance of cancer stem cell properties [22, 23]. The anti-metastatic effects observed with Telomir-Zn in the HCC1806 zebrafish model align with prior findings that copper depletion selectively impairs metastatic dissemination while sparing primary tumor proliferation.

This dual modulation of labile iron and copper pools by Telomir-Zn may therefore offer complementary advantages over iron-only chelators, simultaneously targeting epigenetic regulation (via Fe^{2+}-dependent KDMs) and mitochondrial/metastatic pathways (via Cu^{2+}).

Collectively, these findings suggest that Telomir-Zn may preferentially target tumors with features consistent with iron dependence and epigenetic liability, supporting stratification using established iron-metabolism markers rather than drug response alone.

Conclusion

Selective intracellular Fe^{2+}/Cu^{2+} modulation by Telomir-Zn drives epigenetic reprogramming and exerts antitumor activity in preclinical models of prostate cancer and TNBC. This approach offers a novel therapeutic strategy for targeting metabolic-epigenetic vulnerabilities in aggressive, iron-addicted malignancies.

Abbreviations

API: Active pharmaceutical ingredient

BW: Body weight

CARD: caspase activation and recruitment domain

DFO: Deferoxamine

DNA: Deoxyribonucleic acid

DNMT: DNA methyltransferase

EMT: Epithelial–mesenchymal transition

FBS: Fetal bovine serum

FPN: Ferroportin

HDM: Histone demethylase

IC_{50}: Half-maximal inhibitory concentration

JmjC: Jumonji C domain

KDM: Lysine demethylase

LIP: Labile iron pool

PC-3: Human prostate cancer cell line

PTX : Paclitaxel

PYCARD/ASC: Apoptosis-associated Speck-like protein containing a CARD

qPCR: Quantitative polymerase chain reaction

ROS: Reactive oxygen species

SEM: Standard error of the mean

STAT1: Signal transducer and activator of transcription 1

TNBC: Triple-negative breast cancer

UTX (KDM6A): Ubiquitously Transcribed Tetratricopeptide Repeat on X Chromosome

XTT/WST-1:Tetrazolium-based cell viability assays.

Data Availability: All data generated and analyzed in this study are included in the manuscript and its accompanying figures. The raw data supporting the conclusions of this article will be made available by the authors, without undue reservation.

Ethics Statement: All animal studies were conducted in accordance with institutional guidelines for the care and use of laboratory animals. The PC-3 xenograft study was performed under an approved Institutional Animal Care and Use Committee (IACUC) protocol at Pharmaseed (Nes-Ziona, Israel). All procedures—including tumor implantation, dosing, monitoring, and euthanasia—were performed in accordance with internationally accepted ethical standards for animal research. This study was performed in compliance with "The Israel Animal Welfare Act" and following "The Israel Board for Animal Experiments" Ethics Committee approval # NPC-Ph - IL - 2412 – 524.

Author Contributions: I.A. and E.A. conceived and designed the study. M.G. and R.M. performed the in vitro assays and chelation studies. P.R.H. conducted the in vitro assays and in vivo mouse xenograft experiments. G.V.R and A.E. performed the Zebrafish in vivo experiments. I.A. wrote the manuscript with input from all authors. All authors reviewed and approved the final version of the manuscript.

Funding: This research was supported by Telomir Pharmaceuticals, Inc., which provided funding for in vitro studies, analytical development, and in vivo xenograft experiments.

Acknowledgments: The authors thank the scientific and technical teams at Pharmaseed, Smart Assays Biotechnologies and BioReperia AB for their contributions to the in vivo and in vitro studies. We also acknowledge the support of Telomir Pharmaceuticals, Inc. for project coordination and study oversight.

Conflict of Interest: Erez Aminov is the Chief Executive Officer of Telomir Pharmaceuticals, Inc. Itzchak Angel and other co-authors are consultants, or scientific advisors to the company. Telomir Pharmaceuticals is developing Telomir-Zn. All other authors declare no additional competing financial interests. E.A. is the founder and Chief Executive Officer of Telomir Pharmaceuticals, Inc., I.A. is Chief Scientific Advisor to Telomir Pharmaceuticals and. M.G. and R.M. are employees of Smart Assays Biotechnologies; P.R.H. is an employee of Pharmaseed Ltd.; and G.V.R. and A.E. are employees of BioReperia AB — contract research organizations that received funding from Telomir Pharmaceuticals to conduct the studies described. Telomir Pharmaceuticals is the sponsor of this research and is developing Telomir-Zn, which is covered by the company's intellectual property. The sponsor participated in the study design, data interpretation, and preparation of this manuscript. Beyond the disclosures above, the authors declare no further competing interests.

Citation: Angel I, Gladnikoff M, Hasson PR, Rodriguez GV, Mayer R, et al. (2026) Telomir-Zn Modulates Intracellular Iron and Copper to Inhibit JmjC Histone Demethylases and Suppress Tumor Growth in Prostate and Triple-Negative Breast Cancer. J Oncol Res Ther 11: 10350. DOI: 10.29011/2574-710X.10350.

References

1. Yu X, Zhao H, Wang R, Chen Y, Ouyang X, et al. (2024) Cancer Epigenetics: From Laboratory Studies and Clinical Trials to Precision Medicine. Cell Death Discov 10: 28.
2. Sherif ZA, Ogunwobi OO, Ressom HW (2025) Mechanisms and Technologies in Cancer Epigenetics. Front Oncol 14: 1513654.
3. Marei HE (2025) Epigenetic Regulators in Cancer Therapy and Progression. npj Precis. Oncol 9.
4. Lavoro A, Ricci D, Gattuso G, Longo F, Spoto G, et al. (2025) Recent Advances on Gene-Related DNA Methylation in Cancer Diagnosis, Prognosis, and Treatment: A Clinical Perspective. Clin. Epigenetics 17: 76.
5. Alotaibi, G (2025) A Systematic Review of Progress Toward Unlocking the Power of Epigenetics in Breast Cancer: Latest Updates and Perspectives. Front. Pharmacol 16: 1628165.
6. Ma C, Cheng J, Gu J, Wang Q (2025) Epigenetic Drugs in Cancer Therapy: Mechanisms, Immune Modulation, and Therapeutic Applications. Mol. Biomed 6: 132.
7. Torti SV, Torti FM (2013) Iron and Cancer: More Ore to be Mined. Nat. Rev. Cancer 13: 342-355.
8. Ge EJ, Bush AI, Casini A, Cobine PA, Cross JR, et al. (2022) Connecting Copper and Cancer: From Transition Metal Signalling to Metalloplasia. Nat. Rev. Cancer 22: 102-113.
9. Kooistra SM, Helin K (2012) Molecular Mechanisms and Potential Functions of Histone Demethylases. Nat. Rev. Mol. Cell Biol 13: 297-311.
10. Loenarz C, Schofield CJ (2008) Expanding Chemical Biology of 2-Oxoglutarate Oxygenases. Nat. Chem. Biol. 4: 152-156.
11. Tsukada Y, Fang J, Erdjument-Bromage H, Warren M.E, Borchers C.H, et al. (2006) Histone Demethylation by a Family of JmjC Domain-Containing Proteins. Nature 439: 811-816.
12. Klose RJ, Kallin EM, Zhang Y (2006) JmjC-Domain-Containing Proteins and Histone Demethylation. Nat. Rev. Genet 7: 715-727.
13. Pedersen MT, Helin K (2010) Histone Demethylases in Development and Disease. Trends Cell Biol 20: 662-671.
14. Yang GJ, Zhu MH, Lu XJ, Liu YJ, Lu JF, et al. (2021) The Emerging Role of KDM5A in Human Cancer. J. Hematol. Oncol 14: 30.
15. Jones PA, Issa JPJ, Baylin S (2016) Targeting the Cancer Epigenome for Therapy. Nat. Rev. Genet 17: 630-641.
16. Helin K, Dhanak D (2013) Chromatin Proteins and Modifications as Drug Targets. Nature 502: 480-488.
17. Rodriguez R, Schreiber SL, Conrad M (2022) Persister Cancer Cells: Iron Addiction and Vulnerability to Ferroptosis. Mol. Cell 82: 728-740.
18. Bianchini G, Balko JM, Mayer IA, Sanders ME, Gianni L (2016) Triple-Negative Breast Cancer: Challenges and Opportunities of a Heterogeneous Disease. Nat. Rev. Clin. Oncol 13: 674-690.
19. Podo F, Buydens LMC, Degani H, Hilhorst R, Klipp E, et al. (2010) Triple-Negative Breast Cancer: Present Challenges and New Perspectives. Mol. Oncol 4: 209-229.
20. Mahmoud R, Ordóñez-Morán P, Allegrucci C (2022) Challenges for Triple-Negative Breast Cancer Treatment. Cancers 14: 4280.
21. Torti SV, Torti FM (2020) Iron and Cancer: 2020 Vision. Cancer Res 80: 5435-5448.
22. Ramchandani D, Berisa M, Tavarez DA, Li Z, Miele M, et al. (2021) Copper Depletion Modulates Mitochondrial Oxidative Phosphorylation to Impair Triple Negative Breast Cancer Metastasis. Nat. Commun 12: 7311.
23. Chan N, Willis A, Kornhauser N, Ward MM, Lee SB, et al. (2017) Influencing the Tumor Microenvironment: A Phase II Study of Copper Depletion Using Tetrathiomolybdate in Patients with Breast Cancer at High Risk for Recurrence and in Pre-Clinical Models of Breast Cancer. Clin. Cancer Res 23: 666-676.
24. Abbasi U, Abbina S, Gill A, Bhagat V, Kizhakkedathu JN (2021) A Facile Colorimetric Method for the Quantification of Labile Iron Pool and Total Iron in Cells and Tissue Specimens. Sci. Rep 11: 6008.
25. Keberle H (1964) The Biochemistry of Desferrioxamine and Its Relation to Iron Metabolism. Ann. N.Y. Acad. Sci 119: 758-768.
26. Grubwieser P, Brigo N, Seifert M, Grander M, Theurl I, et al. (2024) Quantification of Macrophage Cellular Ferrous Iron Using a Fluorescent Probe. Bio Protoc 14: e4929.
27. Kristensen LH, Nielsen AL, Helgstrand C, Lees M, Cloos P, et al. (2012) Studies of H3K4me3 Demethylation by KDM5B/Jarid1B/PLU1 Reveals Strong Substrate Recognition in Vitro and Identifies 2,4-pyridine-dicarboxylic acid As an In Vitro and In Cell Inhibitor. FEBS J 279: 1905-1914.
28. Richardson DR, Kalinowski DS, Lau S, Jansson PJ, Lovejoy B (2009) Cancer Cell Iron Metabolism and the Development of Potent Iron Chelators as Anti-Tumour Agents. Biochim. Biophys. Acta 1790: 702-717.
29. Hider RC, Kong XL (2010) Chemistry and Biology of Siderophores. Nat. Prod. Rep 27: 637-657.
30. Tsvetkov P, Coy S, Petrova B, Dreishpoon M, Verma A, et al. (2022) Copper Induces Cell Death by Targeting Lipoylated TCA Cycle Proteins. Science 375: 1254-1261.
31. Maret W (2016) The Metals in the Biological Periodic System of the Elements: Concepts and Conjectures. Int. J. Mol. Sci 17: 66.
32. Lutsenko S (2010) Human Copper Homeostasis: A Network of Interconnected Pathways. Curr. Opin. Chem. Biol 14: 211-217.
33. Kakhlon O, Cabantchik ZI (2002) The Labile Iron Pool: Characterization, Measurement, and Participation in Cellular Processes. Free Radic. Biol. Med 33: 1037-1046.
34. Cotruvo JA, Aron AT, Ramos-Torres KM, Chang CJ (2015) Synthetic Fluorescent Probes for Studying Copper in Biological Systems. Chem. Soc. Rev 44: 4400-4414.
35. Manni W, Jianxin X, Weiqi H, Siyuan C, Huashan S (2022) JMJD Family Proteins in Cancer and Inflammation. Signal Transduct. Target. Ther 7: 365.
36. Zhang, L, Chen, Y, Li, Z, Lin C, Zhang T, et al. (2023) Development of JmjC-Domain-Containing Histone Demethylase (KDM2-7) Inhibitors for Cancer Therapy. Drug Discov. Today 28: 103519.
37. Rose NR, Klose RJ (2014) Understanding the Relationship Between DNA Methylation and Histone Lysine Methylation. Biochim. Biophys. Acta 1839: 1362-1372.
38. Wu X, Zhang Y (2017) TET-Mediated Active DNA Demethylation: Mechanism, Function and Beyond. Nat. Rev. Genet 18: 517-534.
39. Fior R, Povoa V, Mendes RV, Carvalho T, Gomes A, et al. (2017) Single-Cell Functional and Chemosensitive Profiling of Combinatorial Colorectal Therapy in Zebrafish Xenografts. Proc. Natl. Acad. Sci. U.S.A 114: E8234-E8243.

40. Fazio M, Ablain J, Chuan Y, Langenau DM, Zon LI (2020) Zebrafish Patient Avatars in Cancer Biology and Precision Cancer Therapy. Nat. Rev. Cancer 20: 263-273.

41. Dixon SJ, Lemberg KM, Lamprecht MR, Skouta R, Zaitsev EM, et al. (2012) Ferroptosis: An Iron-Dependent Form of Non-Apoptotic Cell Death. Cell 149: 1060-1072.

42. Stockwell BR, Jiang X, Gu W (2020) Emerging Mechanisms and Disease Relevance of Ferroptosis. Trends Cell Biol 30: 478-490.

43. Jiang X, Stockwell BR, Conrad M (2021) Ferroptosis: Mechanisms, Biology and Role in Disease. Nat. Rev. Mol. Cell Biol 22: 266-282.

44. Alothaim T, Charbonneau B, Tang X (2021) HDAC6 Inhibitors Sensitize Non-Mesenchymal Triple-Negative Breast Cancer Cells to Cysteine Deprivation. Sci. Rep 11: 10956.

45. Espinosa Fernandez JR, Eckhardt BL, Lee J, Lim B, Pearson T, et al. (2020) Identification of Triple-Negative Breast Cancer Cell Lines Classified Under the Same Molecular Subtype Using Different Molecular Characterization Techniques. PLoS ONE 15: e0231953.

46. Recalcati S, Locati M, Marini A, Santambrogio P, Zaninotto F, et al. (2010) Differential Regulation of Iron Homeostasis During Human Macrophage Polarized Activation. Eur. J. Immunol 40: 824-835.

47. Ganz T, Nemeth E (2015) Iron Homeostasis in Host Defence and Inflammation. Nat. Rev. Immunol 15: 500-510.

48. Jung M, Mertens C, Brüne B (2015) Macrophage Iron Homeostasis and Polarization in the Context of Cancer. Immunobiology 220: 295-304.

49. Manz DH, Blanchette NL, Paul BT, Torti FM, Torti SV (2016) Iron and Cancer: Recent Insights. Ann. N.Y. Acad. Sci 1368: 149-161.

50. Pinnix ZK, Miller LD, Wang W, D'Agostino Jr, Kute T, et al. (2010) Ferroportin and Iron Regulation in Breast Cancer Progression and Prognosis. Sci. Transl. Med 2: 43ra56.

51. Wang Y, Yu L, Ding J, Chen Y (2019) Iron Metabolism in Cancer. Int. J. Mol. Sci 20: 95.